

Nanoscale

Accepted Manuscript



This is an *Accepted Manuscript*, which has been through the Royal Society of Chemistry peer review process and has been accepted for publication.

Accepted Manuscripts are published online shortly after acceptance, before technical editing, formatting and proof reading. Using this free service, authors can make their results available to the community, in citable form, before we publish the edited article. We will replace this *Accepted Manuscript* with the edited and formatted *Advance Article* as soon as it is available.

You can find more information about *Accepted Manuscripts* in the [Information for Authors](#).

Please note that technical editing may introduce minor changes to the text and/or graphics, which may alter content. The journal's standard [Terms & Conditions](#) and the [Ethical guidelines](#) still apply. In no event shall the Royal Society of Chemistry be held responsible for any errors or omissions in this *Accepted Manuscript* or any consequences arising from the use of any information it contains.

PAPER

Porous single-crystalline palladium nanoflowers with enriched {100} facets for highly enhanced ethanol oxidation

Cite this: DOI: 10.1039/x0xx00000x

Kun Qi,^a Qiyu Wang,^a Weitao Zheng,^{*a} Wei Zhang,^a and Xiaoqiang Cui^{*a}Received 00th January 2012,
Accepted 00th January 2012

DOI: 10.1039/x0xx00000x

www.rsc.org/

Palladium porous single-crystalline nanoflowers (PSNFs) with enriched high catalytic activity {100} facets were synthesized by a mild and controllable seed mediated growth method. The growth mechanism of the Pd PSNFs was investigated by time dependent morphology evolution through TEM imaging. Due to the specific structure, Pd PSNFs show highly enhanced ethanol oxidation reaction (EOR) activity, high EOR anti-poisoning and stability, much better than Pd nanocubes, {111} facets dominated dendritic urchin-like Pd nanoparticles and Pd black.

1. Introduction

Palladium nanoparticles (NPs) have gained great deal of attention in the area of catalysis such as C-C coupling,¹ CO oxidation,² oxygen reduction reaction,³ formic acid oxidation,^{4,5} and also direct alcohol fuel cells.⁶⁻⁸ Optimizing the morphology and crystal structure of Pd NPs can tremendously improve their catalytic activity.⁹ For instance, porous nanostructures have shown great enhancement of the catalytic activity due to high specific surface areas and plentiful atomic steps with high index facets.^{10, 11} Pd porous nanostructures is normally prepared through the aggregation of small nanostructures formed by rapid reduction of the precursor,^{12, 13} or through the seed mediated overgrowth and etching process.^{14, 15} During the reduction of precursor, metallic atoms are randomly arranged on all facets of small nanostructure or preferably deposited onto some high energy sites to form thermodynamically stable facets with the lowest surface energy. {111} facets always encase the lowest surface energy for the case of Pd, which performs face-centered cubic (fcc) metallic nanostructure.¹⁶ Therefore, almost all of the Pd porous nanostructures were either polycrystalline formed by aggregation of small nanostructures or single-crystalline structure with {111} facets dominated rooted in the thermodynamic control growth process.^{17, 18} As the catalytic activity of Pd NPs strongly depend on their exposing facets, in terms of experiments and theoretical simulation, researchers have found that the open Pd {100} facets present a better catalytic activity than closed-packed Pd {111} facets and also the stepped Pd {110} facets in most of the catalytic field.¹⁹⁻²³ Herein, we report a simple route based on seed mediated growth to the synthesis of Pd porous single-crystalline nanoflowers (PSNFs) bounded by enriched {100} facets. To the best of our knowledge, this work provides the first report on a porous single-crystalline Pd nanostructure with high catalytic activity {100} facets dominated. As-prepared Pd PSNFs exhibit significantly enhanced catalytic activity, higher stability and anti-poisonous ability relative to other Pd-based catalysts for electro-oxidation reaction of ethanol owing to their specific structure such as porous, single-crystalline, {100} facets dominated, abundant atomic steps with high-index facets as catalytic active sites.²⁴

2. Experimental

2.1 Material and reagents

Palladium chloride (PdCl₂, 99.999%), FTO (~7 Ω/sq), Hellmanex™ lotion, Pd black (Pd≥99.9%), were obtained from Sigma-Aldrich. Hydrochloric acid (HCl, AR), sulphuric acid (H₂SO₄, AR), ascorbic acid (AA, AR) were obtained from Beijing chemical works, China. H₂PdCl₄ aqueous solution was prepared from hydrochloric acid (HCl) aqueous solution and palladium chloride (PdCl₂). Cetyltrimethyl ammonium bromide (CTAB, AR), cetyltrimethyl ammonium chloride (CTAC, CR), potassium hydroxide (KOH, AR), and ethanol (AR) were all purchased from Sinopharm chemical reagent, China. The water (18.2 MΩ cm⁻¹) used in all experiments was prepared by passing through an ultrapure purification system.

2.2 Synthesis of palladium nanocube seeds

Cubic Pd seeds were synthesized according to a published procedure.²⁵ In a typical synthesis, 45.6 mg of CTAB was dissolved in 10 mL water within a 20 mL vial and heated at 95 °C under magnetic stirring. After 5 min, 0.5 mL of 10 mM H₂PdCl₄ was added. After another 5 min, 80 μL of 0.1 M ascorbic acid solution was quickly added. The reaction was stopped after 10 min and stored at 30 °C for future use.

2.3 Synthesis of palladium porous single-crystalline nanoflowers

In a typical synthesis, 20 mL of 0.1 M CTAB solution was injected into a 40 mL scintillation vial and kept in a 40 °C water bath. Then 250 μL of 10 mM H₂PdCl₄ solution was injected and gently mixed. 5 minutes later, corresponding amount of Pd nanocube seeds was added into the solution. After completely mixed, 400 μL of freshly prepared 0.1 M ascorbic acid solution was injected and the solution was gently mixed. The resulting solution was placed in a water bath at 40 °C without disturbance. After 12 h, when the reaction completed, the

products were collected by centrifugation (12000 rpm, 5 min). The supernatant was discarded and the precipitate was redispersed in 40 °C water. The centrifugation-redispersion procedures were repeated for another two times and the final product was redispersed in 1.5 mL of water. For the 52, 65, 73, and 81 nm porous single-crystalline Pd nanoflowers, 480, 360, 240, and 160 μL of the Pd nanocube seed solution were added respectively.

2.4 Synthesis of palladium large nanocubes

In a typical synthesis, 20 mL of 0.1 M CTAB solution was injected into a 40 mL scintillation vial and kept in a 40 °C water bath. Then 500 μL of 10 mM H_2PdCl_4 solution was injected and gently mixed. To obtain the 65 nm Pd nanocubes, 5 minutes later, 140 μL of Pd nanocube seeds was added into the solution. After completely mixed, 400 μL of freshly prepared 0.1 M ascorbic acid solution was injected and the solution was gently mixed. The resulting solution was placed in a water bath at 40 °C without disturbance. After 12 h, when the reaction completed, the products were collected and washed the same way as the Pd PSNFs.

2.5 Synthesis of palladium urchin-like nanoparticles

In a typical synthesis, 20 mL of 0.1 M CTAC solution was injected into a 40 mL scintillation vial and kept in a 40 °C water bath. Then 250 μL of 10 mM H_2PdCl_4 solution was injected and gently mixed. To obtain the 69 nm Pd urchin-like NPs, 5 minutes later, 360 μL of Pd nanocube seeds was added into the solution. After completely mixed, 400 μL of freshly prepared 0.1 M ascorbic acid solution was injected and the solution was gently mixed. The resulting solution was placed in a water bath at 40 °C without disturbance. After 12 h, when the reaction completed, the products were collected and washed the same way as the Pd PSNFs.

2.6 Characterization

Transmission electron microscope (TEM), high resolution transmission electron microscope (HRTEM), selected area electron diffraction (SAED), scanning transmission electron microscope (STEM), high-angle annular dark-field scanning transmission electron microscopy (HAADF-STEM) images and energy-disperse X-ray (EDX) spectrum were acquired by using a JEM-2100F transmission electron microscope equipped with a high-angle annular dark-field detector (JEOL Co., Japan). X-Ray diffraction (XRD) patterns were obtained by using a Bragg-Brentano diffractometer (D8-tools, Germany), and the source was a Cu-K α line at 0.15418 nm. X-ray photoelectron spectroscopy (XPS) data was acquired with an ESCALAB-250 instrument (Thermo Fisher Scientific, USA), performed with a monochromatic Al-K α (1486.6 eV) radiation source and a hemisphere detector with an energy resolution of 0.1 eV. Inductively coupled plasma mass spectrometry (ICP-MS) data were determined by an ELAN 9000/DRC ICP-MS system. Fast Fourier transform (FFT) contrast refined HRTEM images were obtained by Gatan digital micrograph software. TEM snapshot was achieved by quenching 800 μL of the growth solution by high speed centrifugation (16000 rpm, 1 min) and washed two times with 40 °C deionized water. Finally, 5 μL of solution with suitable concentration was drop-cast onto a carbon supported film and dried at room temperature in an enclosed environment.

2.7 Electrochemical measurements

The electrochemical measurements were conducted by using a CHI650D electrochemical workstation (Shanghai, Chenhua Co., China). A three-electrode cell was equipped with a saturated calomel electrode (SCE) as the reference electrode, a platinum foil electrode (1cm \times 3cm) as the counter electrode and a nanoparticle modified FTO electrode (1cm \times 3cm) as the working electrode. Before modification, the FTO electrode was ultrasonic cleaned with 1% HellmanexTM aqueous solution for two hours and rinsed with great amount of deionized water. Cleaned FTO was then put in a glass garden and the catalyst solution with suitable concentration was uniformly drop-cast onto the surface of FTO electrode. The liquid drop was slowly dried at room temperature in a sealed environment. Before each electrochemical test, the electrode was electrochemically activated in a N_2 saturated 0.5 M H_2SO_4 solution by performing cyclic voltammetry scanning at -0.3–1.2 V for 50 cycles until stable voltammograms were obtained. Ethanol oxidation reaction (EOR) catalytic activity and stability tests were all performed in a N_2 saturated solution containing 1 M KOH (aq) and 1M ethanol. Catalytic activity and cycling stability measurements were all carried out by cyclic voltammetry scanning at -0.9–0.6 V with a scan rate of 50 mV s^{-1} . Long-term stability test was recorded by taking a Chronoamperometric (CA) scanning at a constant potential of -0.2 V. All of the electrochemical tests were performed at room temperature.

3. Results and discussion

3.1 Characterization of Pd PSNFs

Pd PSNFs samples were prepared by a seed mediated epitaxial growth method in aqueous solutions. Pd nanocube seeds (23 \pm 1.9 nm in diameter) were synthesized and characterized according to previous report (Fig. S1).²⁵ The TEM image of the Pd PSNFs indicates that nanoparticles are monodispersed with a flower-like morphology as shown in Fig. 1a. HRTEM image of the Pd PSNFs is displayed in Fig. 1b, which shows the lattice space of the nanostructure is 1.95 Å; inset shows the FFT pattern and FFT contrast refined HRTEM image of the red square area in Fig. 1b, the characteristic square spot array of the FFT pattern and the distinctive square tight atomic arrangement indicate a single-crystalline nature and confirm that the Pd PSNFs are enclosed by {100} facets.^{26, 27} XRD patterns recorded on the Pd-based catalysts were shown in Fig. 1c.

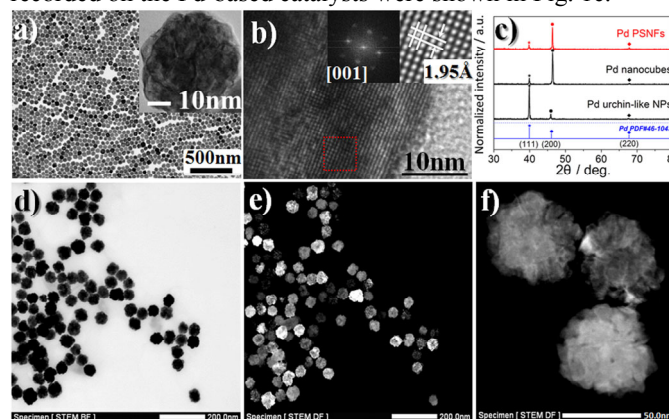


Fig. 1 (a) TEM and (b) HRTEM images of Pd PSNFs; Inset of (a) shows the magnified image of a Pd PSNFs, the inset of (b) shows the corresponding FFT pattern and FFT refined HRTEM image of the region indicated by the red box in (b) recorded along [001] zone axis. (c) XRD pattern of Pd nanostructures. (d–e) Bright field STEM and HAADF-STEM of Pd PSNFs. (f) High magnified HAADF-STEM of Pd PSNFs.

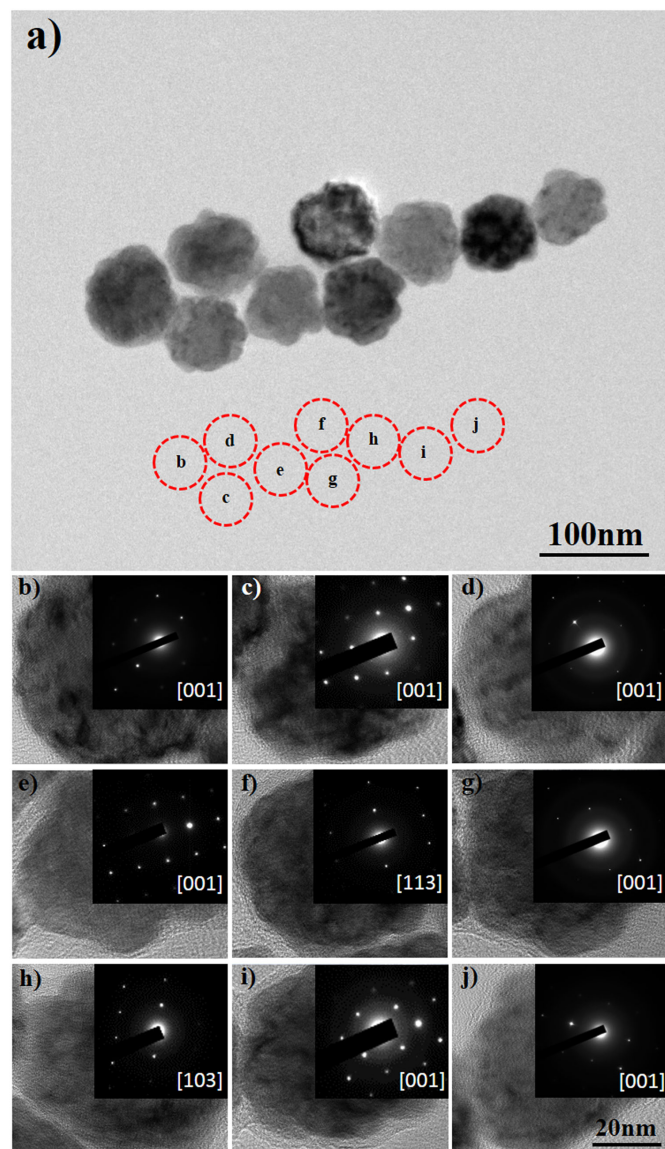


Fig. 2 (a) TEM image of nine Pd PSNFs by random sampling. (b–j) Magnified TEM and SAED images of corresponding Pd PSNFs, all of these SAED patterns were taken from whole individual nanoparticle (scale bars of image b–j are all 20 nm as shown at the right bottom corner).

Peaks located at 40° , 46° and 68° can be indexed to the (111), (200), and (220) planes of fcc palladium, respectively. XRD patterns of the Pd PSNFs and Pd nanocubes show an abnormally intense (200) peak, suggesting a relatively large proportion of these Pd NPs were oriented with their {100} facets parallel to the substrate.²⁸ However, the urchin-like Pd NPs synthesized as described previously with slightly modification was dominated by {111} facets.¹² The corresponding HAADF-STEM images displayed in Fig. 1d–f clearly reveal the porous structure of the Pd PSNFs.²⁹ N_2 sorption measurements were failed to be performed owing to the aggregation and coalescence caused by drying during the measurements. In order to determine the real surface area, we calculated the mass electrochemical active area (ECSA) instead (details are described in SI). Elemental and electronic state analyse of Pd PSNFs are shown in Fig. S2. From the EDX spectrum and XPS data, we can infer that PSNFs are Pd nanoparticles with slight capping agents on their surface. In

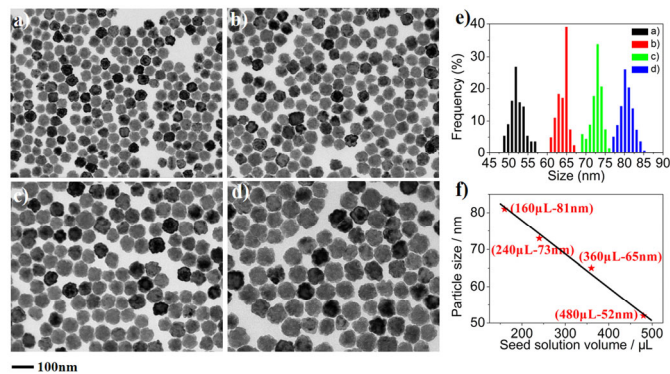


Fig. 3 TEM images of Pd PSNFs with different sizes (Scale bar: 100 nm). (a) 52 ± 2.7 nm. (b) 65 ± 1.9 nm. (c) 73 ± 2.5 nm. (d) 81 ± 2.4 nm. (e) Statistics of the particle diameter distribution of Pd PSNFs with different sizes. (f) Linear relationship curve of Pd nanocube seed solution additive amount and obtained Pd PSNFs size.

order to further demonstrate the single-crystalline nature of the PSNFs, we characterized the crystalline structure of the individual Pd PSNFs with SAED, as shown in Fig. 2. The characteristic square spot arrays of SAED patterns indicate the single-crystalline nature and confirm the Pd PSNFs are enclosed by {100} facets. Fig. S3 shows HRTEM image of a randomly picked Pd PSNF with crystalline grains arranged by the same orientation and unchanged punctiform FFT pattern over the entire nanoparticle, which once again demonstrate the single-crystalline nature.³⁰ The diameter of the Pd PSNFs can be readily controlled by varying the volume of the seed solution, and a linear relationship can be obtained between the size of the PSNFs and the additive seed amount as shown in Fig. 3. For further application of the Pd PSNFs, we calculated the relationship between the seed solution volume and the obtained particle size by formula:

$$(-0.0912) \times V_{\text{seed solution}} (\mu\text{L}) + 96.176 = d_{\text{Pd PSNFs}} (\text{nm}), R=0.99,$$

Where $V_{\text{seed solution}}$ is the volume of seeds addition, $d_{\text{Pd PSNFs}}$ is the diameter of obtained Pd PSNFs.

3.2 Growth mechanism of Pd PSNFs

To better understand the growth mechanism of the Pd PSNFs, we analysed the reaction time dependent morphology evolution by TEM imaging (Fig. 4). TEM snapshot started from 0 minute which is the time point when ascorbic acid was added into the reaction system and reduction of Pd^{2+} began. Fig. 4 and Fig. S4 show the obvious changes of morphology, particle size and solution colour during the reaction. The results show that a fast size increase happens at the initial 20 min while the cubic shape of Pd NPs is retained. At the same time, slight concavity is formed at the six faces of each nanocube. After that, the concave nanocubes change into convex nanocubes and finally transform into spherical flower-like shape with slowly size increase. Based on these observations, we propose a mechanism as shown in Scheme. 1. Where V_1 means the diffusion rate of Pd precursor to nanocube seeds, V_2 indicates the generation rate of Pd atoms and also the consumption rate of Pd precursor on the nanocube surface, V_3 stands for the surface diffusion rate of Pd atoms.^{31, 32} At the beginning, the reaction processes quite fast because of the high precursor concentration as illustrated by the first 15 min state in Fig. 4m. In this state, the rates mentioned above arrange in the order of: $V_1, V_2 > V_3$ due to the relative low reaction temperature and fast addition of the Pd

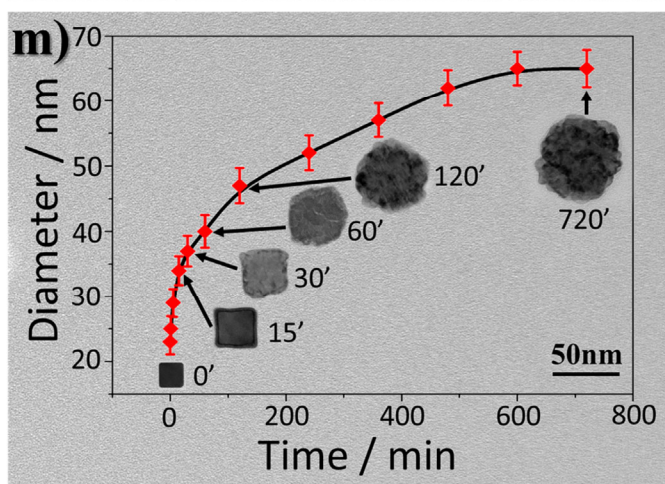
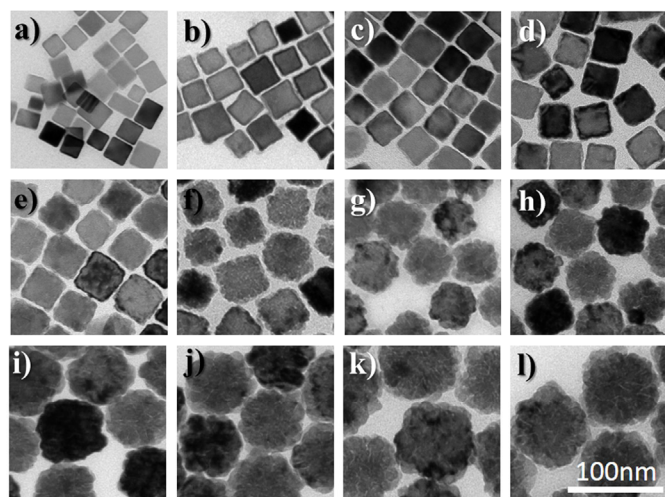
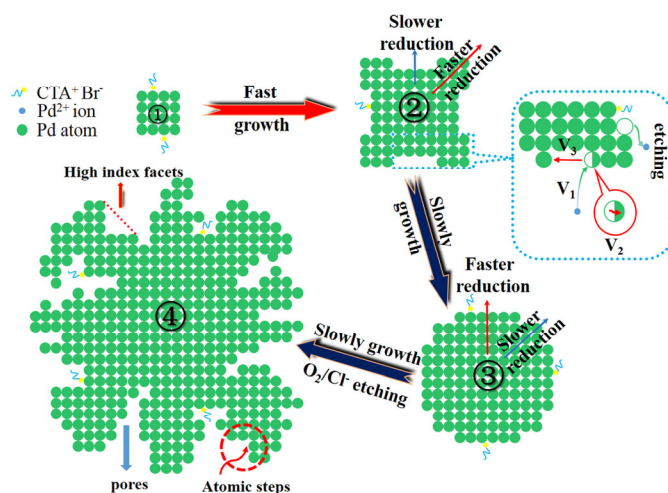


Fig. 4 (a–l) Time dependent morphology evolution of Pd PSNFs. TEM images of the products obtained at: (a) 0 min, (b) 5 min, (c) 15 min, (d) 20 min, (e) 30 min, (f) 45 min, (g) 60 min, (h) 120 min, (i) 240 min, (j) 360 min, (k) 480 min, (l) 720 min. (scale bars of image a–l are all 100 nm as shown at the right bottom corner). (m) The diameter increasing profile and morphological transformation of singular crystal grain indicate the growth mechanism of the Pd PSNFs.

precursor and reductant similar to previously discussed by Xia *et al.*³¹ Meanwhile, $\{100\}$ facets are covered by Br^- ion, therefore most of the Pd atoms will deposit onto the corner sites where $\{111\}$ and $\{110\}$ facets are exposed, generating Pd concave nanocubes as shown in Fig. 4a–4c.³² The total precursor concentration declines dramatically within 20 min during the formation of the concave nanocubes. Then there will be a gradient of the precursor concentration between the convex and concave area due to the different reduction rate and low diffusion rate of the precursor. In this state, the concave area possesses a higher precursor concentration relative to the convex area. Therefore, the growth rate of concave area increases significantly and the nanoparticles begin to grow into convex nanocubes as shown in Fig. 4d–4f. Meanwhile, porous nanostructure starts to form as indicated by the uneven contrast of the nanoparticles because of the insufficient precursor supply as well as etching effects.³³ The concentration of the precursor always declines and finally reaches a growth rate balance, then spherical nanostructures are finally formed as shown in Fig. 4g–4l. Abundant atomic steps with high index facets (indicated by the arrows) were also observed in this $\{100\}$ facets enriched porous nanostructure as shown in Fig. 5, which should be



Scheme. 1 Proposed growth mechanism of Pd PSNFs.

important for the improvement of catalytic activity. No obvious high-index facets can be observed for the commercial Pd black nanoparticles, as shown in Fig. S5.

Two control experiments were also performed to elucidate the reasons of Pd PSNFs performing single-crystalline and mainly $\{100\}$ facets exposing. The first one is disrupting the O_2/Cl^- etching pair by saturating the reaction solution with argon (Ar).³⁴ Previous works reveal that single-crystalline structure were always formed by the assistance of etching, in which particles with enriched lattice defects and stacking faults could be selectively removed.³⁵ In order to reveal the reason for the formation of single-crystalline nature of Pd PSNFs, we carried out a control experiment with O_2/Cl^- etching pair disrupted by saturating the growth solution with Ar. These Pd nanostructures show similar spherical flower like morphology as Pd PSNFs (Fig. 6a). HRTEM images of three randomly selected nanoparticles and corresponding live FFTs over each singular nanoparticle are shown in Fig. 6b–6d. The results show that there are many stacking faults and lattice defects, as indicated by FFT refined HRTEM image (inset of Fig. 6b). FFT patterns are varying from different areas of a singular nanoparticle as shown in the left bottom of Fig. 6b–6d. Above-mentioned results clearly indicate that the presence of O_2/Cl^- etching pair is essential for obtaining single-crystalline nanostructures. The single-crystalline Pd PSNFs nanostructures show higher catalytic activity than that with stacking faults synthesized in Ar saturated growth solution, as shown by the inset of Fig. 6d. The second control experiment is replacing CTAB with CTAC as the capping agent while the other

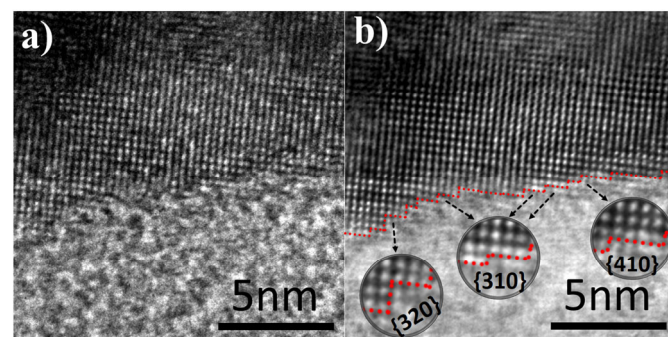


Fig. 5 (a) HRTEM and (b) FFT contrast refined HRTEM image of Pd PSNFs. Inset in (b) clearly shows the atomic steps with high-index facets exposed on the surface.

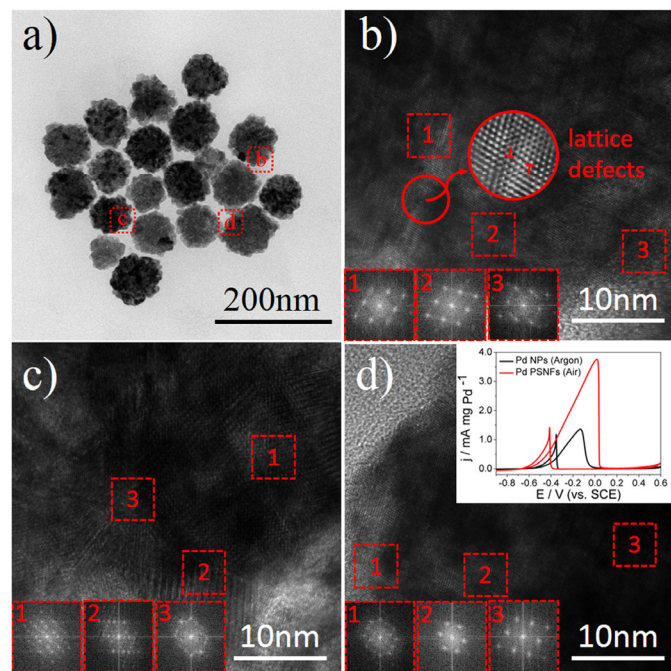


Fig. 6 (a) TEM image of Pd nanoparticles prepared in Ar saturated growth solution and (b–d) HRTEM images from randomly selected areas indicated in (a). The bottom of (b–d) show the live FFT patterns from three areas of each singular Pd nanoparticle. Inset of (b) shows FFT refined HRTEM image of the Pd nanoparticle with obvious lattice defects; inset of (d) shows EOR activity comparison of Pd nanostructures synthesized in air and Ar.

parameters are kept exactly the same. In this non- Br^- ion case, the dendritic urchin-like Pd NPs with $\{111\}$ facets dominated were obtained similar as previous reported results by Yan's group,¹² as shown in Fig. 7a–7c. The size of urchin-like Pd NPs (69 nm, inset of Fig. 7b) is larger than Pd PSNFs (65 nm) in the similar growing environment, which can be interpreted as the difference between dendritic and porous nanostructures. The structure distinction also leads to much more inhomogeneous statistical size distribution of urchin-like NPs than PSNFs. By comparing the growth process and crystalline structure of Pd PSNFs and Pd urchin-like NPs, we can reveal the importance of CTAB as the capping agent for the preparation. The reaction without Br^- ion in the process ran very fast and performed obvious color change within 10 minutes. From the XRD (Fig. 1c) and HRTEM analysis, we can conclude that Pd urchin-like NPs are enclosed by $\{111\}$ facets, which is different from the $\{100\}$ facets dominated Pd PSNFs. All above indicates that Br^- ion in CTAB is essential for the synthesis of $\{100\}$ facets enriched nanostructures in this study.³⁶ The combination of reaction kinetic and thermodynamic controls Pd nanocube-mediated epitaxial growth process and determines the morphology of the obtained nanoparticles, as indicated by Scheme 2. Pd nanocube seeds are prepared in CTAB solution, in which Br^- ion is capping on the $\{100\}$ facets. When the epitaxial growth takes place in CTAB solution, the reaction still goes in kinetic control.³⁷ The mechanism of growth at high precursor concentration is same as the synthesis of Pd seeds, bigger nanocubes are formed in this case (Fig. 7d–7f).³⁸ The concentration gradient in the growth process at low precursor concentration will result in the formation of Pd PSNFs as discussed in Scheme 1. When the epitaxial growth takes place in CTAC solution, the reaction will go in the thermodynamic control. Pd urchin-like nanoparticles with $\{111\}$ facets

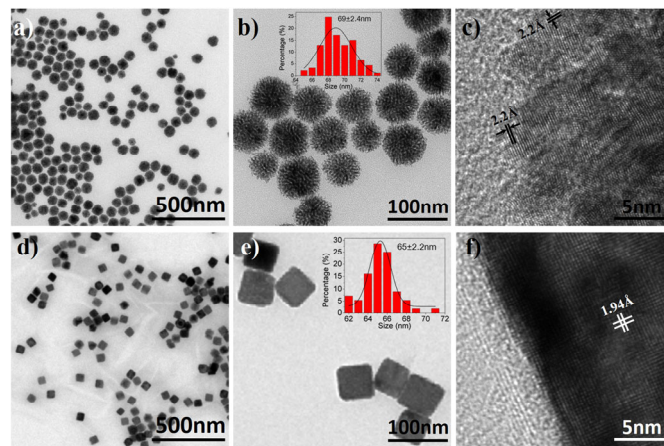
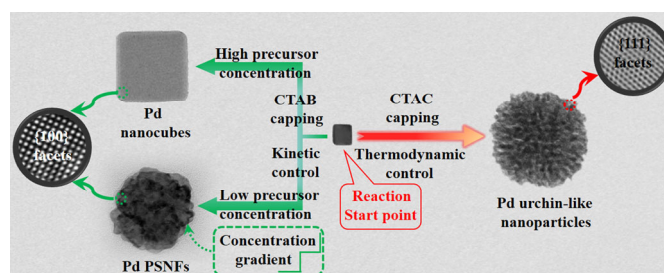


Fig. 7 (a–b) TEM and (c) HRTEM image of Pd urchin-like nanoparticles. The inset in (b) shows the particle diameter distribution. (d–e) TEM and (f) HRTEM image of large Pd nanocubes. The inset in (e) shows the particle diameter distribution.



Scheme. 2 Schematic illustration of three typical growth modes of Pd nanostructures at Pd nanocube seed mediated epitaxial growth condition.

dominated were synthesized in this situation.¹²

3.3 Electrocatalytic property test of Pd PSNFs for EOR

The electrocatalytic activity of as-prepared Pd PSNFs for ethanol oxidation was investigated in an alkaline solution. To remove the excessive CTAB which may bind to the facets of nanoparticles, electrochemical cleaning process were performed before EOR measurement, details are described in Fig. S6. We chose other three

Table 1. Mass ECSA and electrochemical roughness data of Pd-based catalysts.

Catalyst	Mass ECSA [$\text{cm}^2 \text{mg}_{\text{Pd}}^{-1}$]	Roughness ^{a)}
Pd PSNFs (81nm)	475.56	2.50
Pd PSNFs (65nm)	669.59	3.52
Pd PSNFs (52nm)	615.17	3.42
Pd nanocubes (65nm)	370.93	1.95
Pd urchin-like NPs (69nm)	340.16	1.73
Pd black	352.14	1.79

^{a)} Roughness = Active surface area/Geometric area.

kinds of Pd-based catalysts for EOR activity comparison: Pd black ($\text{Pd} \geq 99.9\%$), Pd nanocubes (65 ± 2.1 nm) dominated by $\{100\}$ facets without porosity and Pd urchin-like NPs (69 ± 2.4 nm) enclosed by $\{111\}$ facets with porosity. TEM characterizations of three kinds of Pd-based catalysts are shown in Fig. 7. Mass specific activities of all catalysts were evaluated based on the Pd contents obtained by ICP-MS (ICP-MS and yield data are summarized in Table S1). Mass ECSA and electrochemical roughness data were illustrated in Fig. S7

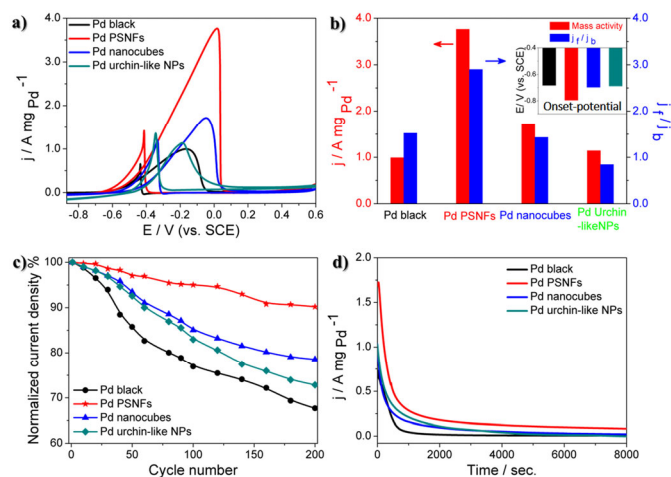


Fig. 8 Electrochemical experimental data: (a) Cyclic voltammograms of four kinds of Pd-based catalysts recorded at room temperature in a solution containing 1 M ethanol and 1 M KOH (aq) with a sweep rate of 50 mV s^{-1} . (b) Mass activity and j_f/j_b for the ethanol oxidation on four different types of catalysts, inset shows the onset-potential comparison for corresponding catalysts. (c) EOR cycling stability of the catalysts with a cycle number of 200. (d) Chronoamperometric curves of four Pd-base catalysts modified electrodes recorded at applied potential of -0.2 V . The currents were normalized by corresponding mass of Pd on each electrode.

and Table 1 (the details for calculation of electrochemical roughness are shown in Table S2). It is shown that Pd PSNFs exhibit the maximum mass ECSA and electrochemical roughness corresponding to the highest catalytic activity. As a probe reaction, EOR was carried out to investigate the catalytic activity. EOR is characterized by well-separated anodic peaks in the forward and backward scans. The magnitude of the forward scan peak current density (j_f) is directly proportional to the amount of ethanol oxidized at the electrode, and the ratio of forward scan peak current density to backward scan peak current density (j_f/j_b) indicate the anti-poisoning ability of catalysts. Anodic peak onset-potential reveals the kinetics of the EOR.³⁹ Blank cyclic voltammograms recorded in 1M KOH (aq.) display no obvious oxidation peak are shown in Fig. S8. Fig. 8a shows the cyclic voltammograms for four kinds of Pd-based catalysts in EOR. The amplified onset potential areas of CVs are shown in Fig. S9 for better observation. Fig. 8b shows the statistical data of mass activity, ratio of forward scan peak current density to backward scan peak current density and the onset-potential (inset of Fig. 8b). Pd PSNFs still exhibit great enhancement for EOR with higher forward scan mass specific peak current density ($3.761 \text{ A mg Pd}^{-1}$), more negative onset-potential (-0.796 V vs. SCE), and high j_f/j_b value (2.913) owe to its specific structure. In order to examine the intrinsic activity of these Pd-based catalysts, ECSA specific activity data were also shown in Fig. S10. It shows that Pd PSNFs possess enhanced ECSA specific activity than other three Pd nanocatalysts with the highest peak current density of 5.64 mA cm^{-2} . The EOR peak potential on Pd PSNFs is 0.12 V more positive than that on Pd black. This is maybe due to the possibility that the active sites are covered by trace capping agent ions on Pd PSNFs, which to some extent, hinder the adsorption of ethanol molecules or hydroxyl species on the Pd surface, and therefore delayed the formation of Pd-OH or Pd-C₂H₅OH, consequently render the EOR at a higher potential.^{40,41} To evaluate the electrocatalytic stability of the catalysts under continuous operating conditions, EOR cycling stability and long-term stability experiments were carried out.^{42,43} Cycling stability curves in Fig. 8c reveal that Pd PSNFs give a better stability than other catalysts with a 90.19% remaining current density after 200 cycles scanning, which is much higher than 78.55%, 72.85% and 67.96% for Pd nanocubes, Pd urchin-like NPs and Pd black catalyst,

respectively. Long-term stability was demonstrated by showing the CA curves recorded at -0.2 V for 8000 seconds in Fig. 8d. After 8000 seconds running, the Pd PSNFs remain a higher current density than other three Pd-based catalysts, which implies a better long-term stability. Relationship between particle size and EOR activity were also investigated by preparing three sizes (52 ± 2.7 , 65 ± 1.9 , and $81 \pm 2.4 \text{ nm}$) of Pd PSNFs, as shown in Fig. S11, middle sized 65nm Pd PSNFs exhibit the highest EOR activity because of the synergistic effect by size and porosity of the catalyst.¹² We compare the mass ECSA and the electrochemical roughness of Pd PSNFs with different size and the data are illustrated in Table 1. Pd PSNFs with the size of 65nm shows the highest mass ECSA and electrochemical roughness which indicates the largest catalyst activity area per unit mass Pd. The result reveals that the 65nm Pd PSNFs have the highest porosity and matches well with our supposition. The highly enhanced catalytic activity can be ascribed to the high specific surface area, enriched EOR activity {100} facets and sufficient accessible atomic steps with high index facets as active sites.⁴⁴⁻⁴⁷ The high electrocatalytic stability can be boiled down to the nanostructure pore confinement efficiency which can enhance both of the cycle and long-term stability.⁴⁸

4. Conclusions

In summary, we have demonstrated a simple, facile, and size controllable seed mediated growth approach for the fabrication of palladium porous single-crystalline nanoflowers contain enriched high catalytic activity {100} facets and atomic steps with high-index-facets as active sites that present significantly enhanced electrocatalytic activity, high anti-poisoning and stability toward ethanol oxidation in alkaline media. The forming mechanism of the Pd PSNFs was investigated based on the study of time-dependent morphology evolution by TEM imaging during the growth process. The present work provides a facile method to the synthesis of porous Pd-based catalyst dominated by desired high catalytic activity facets and demonstrates their potential applications in catalysis.

Acknowledgements

This work was financially supported by the National Natural Science Foundation of China (No. 21275064, 21075051), Program for New Century Excellent Talents in University (NCET-10-0433), Specialized Research Fund for the Doctoral Program of Higher Education (20130061110035)

Notes and references

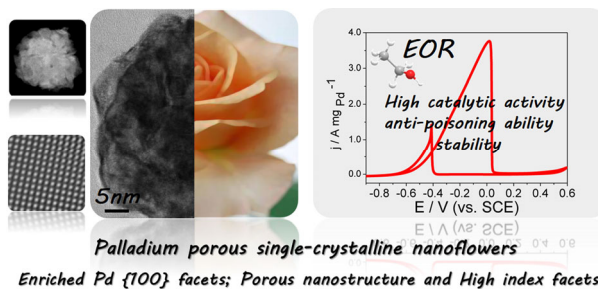
^a Department of Materials Science, Key Laboratory of Automobile Materials of MOE and State Key Laboratory of Superhard Materials, Jilin University, Changchun 130012 People's Republic of China. Tel & Fax: +86-431-85155279, E-mail address: xqcui@jlu.edu.cn (XQ Cui), wtzhang@jlu.edu.cn (WT Zheng)

† Footnotes should appear here. These might include comments relevant to but not central to the matter under discussion, limited experimental and spectral data, and crystallographic data.

Electronic Supplementary Information (ESI) available: [details of any supplementary information available should be included here]. See DOI: 10.1039/b000000x/

1. L. Shao, B. Zhang, W. Zhang, S. Y. Hong, R. Schloegl and D. S. Su, *Angew. Chem. Int. Ed.*, 2013, 52, 2114-2117.
2. Z.-N. Xu, J. Sun, C.-S. Lin, X.-M. Jiang, Q.-S. Chen, S.-Y. Peng, M.-S. Wang and G.-C. Guo, *ACS Catal.*, 2013, 3, 118-122.
3. L. Xiao, L. Zhuang, Y. Liu, J. Lu and H. D. Abruna, *J. Am. Chem. Soc.*, 2009, 131, 602-608.
4. X. Wang, J. Yang, H. Yin, R. Song and Z. Tang, *Adv. Mater.*, 2013, 25, 2728-2732.
5. H. Zhao, J. Yang, L. Wang, C. Tian, B. Jiang and H. Fu, *Chem. Commun.*, 2011, 47, 2014-2016.
6. H. Wu, H. Li, Y. Zhai, X. Xu and Y. Jin, *Adv. Mater.*, 2012, 24, 1594-1597.
7. C. Bianchini and P. K. Shen, *Chem. Rev.*, 2009, 109, 4183-4206.
8. S. J. Ye, D. Y. Kim, S. W. Kang, K. W. Choi, S. W. Han and O. O. Park, *Nanoscale*, 2014, 6, 4182-4187.
9. S. Cheong, J. D. Watt and R. D. Tilley, *Nanoscale*, 2010, 2, 2045-2053.
10. B. Lim, M. Jiang, P. H. C. Camargo, E. C. Cho, J. Tao, X. Lu, Y. Zhu and Y. Xia, *Science*, 2009, 324, 1302-1305.
11. X. Huang, Y. Li, Y. Chen, E. Zhou, Y. Xu, H. Zhou, X. Duan and Y. Huang, *Angew. Chem. Int. Ed.*, 2013, 52, 2520-2524.
12. Y. Feng, X. Ma, L. Han, Z. Peng and J. Yang, *Nanoscale*, 2014, 6, 6173-6179.
13. N. Ortiz and S. E. Skrabalak, *Angew. Chem. Int. Ed.*, 2012, 51, 11757-11761.
14. F. Wang, C. Li, L.-D. Sun, C.-H. Xu, J. Wang, J. C. Yu and C.-H. Yan, *Angew. Chem. Int. Ed.*, 2012, 51, 4872-4876.
15. J.-W. Xiao, S.-X. Fan, F. Wang, L.-D. Sun, X.-Y. Zheng and C.-H. Yan, *Nanoscale*, 2014, 6, 4345-4351.
16. B. Lim, M. Jiang, J. Tao, P. H. C. Camargo, Y. Zhu and Y. Xia, *Adv. Funct. Mater.*, 2009, 19, 189-200.
17. W. Hong, Y. Fang, J. Wang and E. Wang, *J. Power Sources*, 2014, 248, 553-559.
18. A. Mohanty, N. Garg and R. Jin, *Angew. Chem. Int. Ed.*, 2010, 49, 4962-4966.
19. M. H. Ab Rahim, M. M. Forde, R. L. Jenkins, C. Hammond, Q. He, N. Dimitratos, J. A. Lopez-Sanchez, A. F. Carley, S. H. Taylor, D. J. Willock, D. M. Murphy, C. J. Kiely and G. J. Hutchings, *Angew. Chem. Int. Ed.*, 2013, 52, 1280-1284.
20. E. D. Wang, J. B. Xu and T. S. Zhao, *J. Phys. Chem. C*, 2010, 114, 10489-10497.
21. G. Collins, M. Schmidt, C. O'Dwyer, J. D. Holmes and G. P. McGlacken, *Angew. Chem. Int. Ed.*, 2014, 53, 4142-4145.
22. M. H. Shao, T. Yu, J. H. Odell, M. S. Jin and Y. N. Xia, *Chem. Commun.*, 2011, 47, 6566-6568.
23. R. Long, K. Mao, X. Ye, W. Yan, Y. Huang, J. Wang, Y. Fu, X. Wang, X. Wu, Y. Xie and Y. Xiong, *J. Am. Chem. Soc.*, 2013, 135, 3200-3207.
24. L. Y. Chang, A. S. Barnard, L. C. Gontard and R. E. Dunin-Borkowski, *Nano Lett.*, 2010, 10, 3073-3076.
25. W. Niu, W. Zhang, S. Firdoz and X. Lu, *Chem. Mater.*, 2014, 26, 2180-2186.
26. H. Zhang, M. Jin, Y. Xiong, B. Lim and Y. Xia, *Acc. Chem. Res.*, 2012, 46, 1783-1794.
27. W. Niu and G. Xu, *Nano Today*, 2011, 6, 265-285.
28. W. Niu, Z.-Y. Li, L. Shi, X. Liu, H. Li, S. Han, J. Chen and G. Xu, *Cryst. Growth Des.*, 2008, 8, 4440-4444.
29. M. P. Klein, B. W. Jacobs, M. D. Ong, S. J. Fares, D. B. Robinson, V. Stavila, G. J. Wagner and I. Arslan, *J. Am. Chem. Soc.*, 2011, 133, 9144-9147.
30. J. Zhang, C. Feng, Y. Deng, L. Liu, Y. Wu, B. Shen, C. Zhong and W. Hu, *Chem. Mater.*, 2014, 26, 1213-1218.
31. M. Jin, H. Zhang, Z. Xie and Y. Xia, *Angew. Chem. Int. Ed.*, 2011, 50, 7850-7854.
32. S. Xie, S.-I. Choi, N. Lu, L. T. Roling, J. A. Herron, L. Zhang, J. Park, J. Wang, M. J. Kim, Z. Xie, M. Mavrikakis and Y. Xia, *Nano Lett.*, 2014, 14, 3570-3576.
33. J. Liu and D. F. Xue, *Nanoscale Res. Lett.*, 2010, 5, 1525-1534.
34. Y. J. Xiong, J. Y. Chen, B. Wiley, Y. N. Xia, S. Aloni and Y. D. Yin, *J. Am. Chem. Soc.*, 2005, 127, 7332-7333.
35. Y. Zheng, J. Zeng, A. Ruditskiy, M. Liu and Y. Xia, *Chem. Mater.*, 2013, 26, 22-33.
36. Y. Xiong and Y. Xia, *Adv. Mater.*, 2007, 19, 3385-3391.
37. L. Zhang, W. Niu, J. Zhao, S. Zhu, Y. Yuan, T. Yuan, L. Hu and G. Xu, *Faraday Discuss.*, 2013, 164, 175-188.
38. H. Zhang, M. S. Jin and Y. N. Xia, *Angew. Chem. Int. Ed.*, 2012, 51, 7656-7673.
39. C. Hu, H. Cheng, Y. Zhao, Y. Hu, Y. Liu, L. Dai and L. Qu, *Adv. Mater.*, 2012, 24, 5493-5498.
40. Z. Liang, T. Zhao, J. Xu and L. Zhu, *Electrochim. Acta*, 2009, 54, 2203-2208.
41. F. Saleem, Z. Zhang, B. Xu, X. Xu, P. He and X. Wang, *J. Am. Chem. Soc.*, 2013, 135, 18304-18307.
42. C. Hu, X. Zhai, Y. Zhao, K. Bian, J. Zhang, L. Qu, H. Zhang and H. Luo, *Nanoscale*, 2014, 6, 2768-2775.
43. A. L. Wang, H. Xu, J. X. Feng, L. X. Ding, Y. X. Tong and G. R. Li, *J. Am. Chem. Soc.*, 2013, 135, 10703-10709.
44. L. Wang and Y. Yamauchi, *J. Am. Chem. Soc.*, 2013, 135, 16762-16765.
45. Z. Y. Zhou, Z. Z. Huang, D. J. Chen, Q. Wang, N. Tian and S. G. Sun, *Angew. Chem. Int. Ed.*, 2010, 49, 411-414.
46. N. Tian, Z. Y. Zhou, S. G. Sun, Y. Ding and Z. L. Wang, *Science*, 2007, 316, 732-735.
47. Z. Quan, Y. Wang and J. Fang, *Acc. Chem. Res.*, 2013, 46, 191-202.
48. C. Galeano, J. C. Meier, V. Peinecke, H. Bongard, I. Katsounaros, A. A. Topalov, A. Lu, K. J. J. Mayrhofer and F. Schueth, *J. Am. Chem. Soc.*, 2012,

Table of contents



Palladium porous single-crystalline nanoflowers dominated by {100} facets with highly enhanced ethanol oxidation reaction activity, high anti-poisoning and stability were synthesized.